

In situ formation of $MnO_2/Ni(OH)_2$ @nickel foam with porous architecture for triggering persulfate-based advanced oxidation process

Fang Zhu

Changzhou University

Qixing Xiao

Changzhou University

Zihao Hu

Changzhou University

Jianfeng Ma (✉ jma@zju.edu.cn)

Changzhou University

Sridhar Komarneni

The Pennsylvania State University

Yu Mei

Changzhou University

Research Article

Keywords: $MnO_2/Ni(OH)_2$, Nickel foam, Sulfate radical, potassium persulfate

Posted Date: April 18th, 2022

DOI: <https://doi.org/10.21203/rs.3.rs-1540915/v1>

License:   This work is licensed under a Creative Commons Attribution 4.0 International License.

[Read Full License](#)

Abstract

$\text{MnO}_2/\text{Ni}(\text{OH})_2$ was grown in situ on three-dimensional nickel foam (NF), which was then used to activate potassium persulfate (PS) for orange II (OII) degradation. The structure and morphology of the prepared materials were characterized by X-ray diffraction (XRD), field emission scanning electron microscopy (FE-SEM) and transmission electron microscopy (TEM). The removal efficiency of OII was 98.68% with $\text{MnO}_2/\text{Ni}(\text{OH})_2@NF/PS$ system in 40 min. The three-dimensional hierarchical structure of mesoporous material promoted the efficient and fast electron transfer during catalytic activity. Based on classical quenching experiments and the electron spin resonance (ESR) experiments, $\cdot\text{OH}$ and $\text{SO}_4^{\cdot-}$ were identified as the active species in $\text{MnO}_2/\text{Ni}(\text{OH})_2/NF/PS$ system for OII degradation and a degradation mechanism was proposed for this system. Compared with traditional micro-nano particle catalysts, 3D $\text{MnO}_2/\text{Ni}(\text{OH})_2@NF$ has the advantages of convenient recovery and good stability. $\text{MnO}_2/\text{Ni}(\text{OH})_2@NF$ catalyst could be recycled for at least three times, and the degradation rate was 89.06% after three cycles. This $\text{MnO}_2/\text{Ni}(\text{OH})_2@NF$ is expected to be used as a green heterogeneous catalyst.

1 Introduction

In the past several decades, nano-materials and technologies for advanced water treatment have attracted a lot of attention in academic and industrial circles. In the actual water treatment process, nano-materials often have bottlenecks such as easy agglomeration and deactivation, difficult operation, potential safety risks, etc. One of the most effective strategies to deal with these bottlenecks is by using large-size inert carriers to fix nano-particles and prepare composite nano-materials with confined structure. Studies in chemistry, materials science and other related disciplines show that nano-materials after confinement are often significantly different from bulk materials in structure and performance[1, 2], that is, nano confinement effect[1]. This effect has also been partially confirmed in the research of advanced water treatment, but the scientific mechanism research on confinement effect of composite nano-materials in water treatment is just in its infancy[3].

Advanced oxidation technology based on persulfate activation (PS-AOP) has attracted much attention because of its high removal efficiency, simple operation and strong versatility[4–6]. Many studies have shown that hydroxyl radicals and sulfate radicals are the key species to activate persulfate (PS) systems[7]. However, PS-AOP technology still faces challenges such as low selectivity of target pollutants removal and difficult catalyst recovery, both of which limit the practical application of PS-AOP. Therefore, it is necessary to explore a suitable catalyst carrier to solve the problems of catalyst recovery and surface area increase. Because of its three-dimensional channel and good thermal conductivity, metal foam has attracted extensive attention for use as catalyst carriers in various fields [8–10].

Ever increasing number of research papers on activation and application of persulfate indicate that sulfate-radical ($\text{SO}_4^{\cdot-}$) based Advanced Oxidation Processes (SR-AOP) have been widely studied in recent years. Persulfate activation can generate sulfate-radicals through ultraviolet irradiation, heat or metals,

and the latter constitutes a new oxidation technology[11, 12]. Although cobalt/PMS systems were proved to be the most effective way to produce sulfate-radicals[6, 13], cobalt with high toxicity was easy to leach out in homogeneous and heterogeneous reactions, which is a disadvantage as it might cause secondary pollution. Therefore, the application of sulfate radicals produced by non-cobalt-based heterogeneous catalysts in environmental remediation is particularly useful[14].

Polyvalent manganese oxides are abundant in natural environments such as soil, ocean, rocks and fresh water, usually in the form of oxides of manganese (II), manganese (III) and manganese (IV), which are environmentally friendly and far less toxic than cobalt ions[15]. Manganese oxide has the advantages of low cost, easy availability, good environmental compatibility, high catalytic activity and so on, and is expected to be a substitute for cobalt-based catalysts[16]. Ni is the ninth most abundant element in the Earth's crust and has a lower toxicity than Co, and hence Ni-based materials have attracted special attention to activate PS or PMS and proved to be efficient catalysts. The synthesis method of nickel hydroxide ($\text{Ni}(\text{OH})_2$) is simple and has a broad application prospect in catalytic system. Yue et al.[17] first demonstrated the role of $\alpha\text{-Ni}(\text{OH})_2$ as a highly effective nickel-based heterogeneous catalyst for sulfate radical activation.

The monolithic catalyst with three-dimensional hierarchical structure can not only keep the bulk materials easy to separate and reduce the secondary pollution caused by leaching of metal ions, but also avoid the agglomeration of micro/nano particles and expose more active sites, thus significantly improving the catalytic performance[18]. Among many porous foam materials, nickel foam (NF) has high application value because of its unique advantages, including three-dimensional interconnected texture, outstanding mechanical firmness, heat resistance, low economic cost and good environmental stability[19, 20].

As far as we know, previously reported $\text{Ni}(\text{OH})_2$ or $\text{MnO}_2/\text{Ni}(\text{OH})_2$ Nanomaterials on NF were mainly designed for supercapacitors[21–23], but the catalytic performance of hybrids for persulfate has never been investigated. Herein, we report a very simple, low temperature and green route to prepare $\text{Ni}(\text{OH})_2$ nanosheets and MnO_2 nano flowers at the same time on the surface of NF by in situ oxidation-reduction method. The morphology, crystal structure and specific surface area of the catalyst were characterized. The obtained catalyst showed excellent activity and good stability in peroxodisulfate-based Fenton-like reactions. In addition, the mechanism of catalytic oxidation of OII by $\text{MnO}_2/\text{Ni}(\text{OH})_2/\text{NF}/\text{PS}$ heterogeneous system was further studied.

2 Experimental

2.1 Materials and reagents

Nickel foam (NF) (porosity 95%, pore size 0.23 mm) was purchased from Suzhou Kesheng and Metal Materials Company. $\text{MnCl}_2 \cdot 4\text{H}_2\text{O}$, methanol (CH_3OH , MeOH) and H_2O_2 were purchased from Shanghai Titan Scientific Co., Ltd. (Shanghai, China) and used for preparing $\text{MnO}_2/\text{Ni}(\text{OH})_2@/\text{NF}$. Potassium

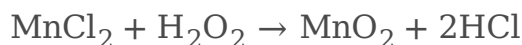
persulfate $K_2S_2O_8$ (PS), p-benzoquinone (BQ) and tert-butyl alcohol (TBA) were obtained from Shanghai Aladdin Biochemical Technology Co., Ltd. (Shanghai, China). Ultrapure water was used in all the experiments.

2.2 Preparation of material

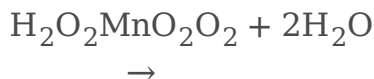
3D NF sheet (Fig. 1 (a)) was first cut to a size of 2 cm × 2 cm × 0.16 cm and was ultrasonically cleaned in 6 mM HCl for 30 min followed by absolute ethanol and deionized water for 15 and 15 minutes. Thus, clean 3D NF sheet (Fig. 1 (b)) was obtained and it was then placed in the Teflon liner of 100 mL stainless-steel hydrothermal vessel.

Then, $MnCl_2 \cdot 4H_2O$ with molar mass of 198 g/mol, 44 mL deionized water and 6 mL 30% H_2O_2 solution were added into 100 mL beaker, and magnetically stirred for 30 min to form a light pink transparent precursor solution. The precursor solution was added into the Teflon liner of hydrothermal vessel. The hydrothermal vessel was sealed and treated at 90°C for 3 h in an oven. The hydrothermal vessel was removed from oven and naturally cooled to room temperature. Then the autoclave was opened, and it was found that except for the foam nickel which changed from silver to black as shown in Fig. 1c below and the rest was a light green transparent solution. The surface of foamed nickel was rinsed with ultrapure water until the solution is neutral, and dried at 80°C for 12 h to obtain $MnO_2/Ni(OH)_2@NF$ material (Fig. 1 (c)). In order to obtain the highest catalytic efficiency of $MnO_2/Ni(OH)_2@NF$ material, the synthesis conditions were optimized by changing the amount of raw materials, hydrothermal temperature and the amount of H_2O_2 . When the reaction temperature was lower than 90°C, the characteristic peaks of $Ni(OH)_2$ could not be found in the synthesized sample, which indicated that the temperature was too low. Although higher reaction temperatures (100°C and 110°C) were also investigated, the three-dimensional reticulated skeleton of NF prepared at these temperatures became less firm and was easily crushed under subsequent stirring.

It is inferred from the experimental phenomena observed during the preparation of $MnO_2/Ni(OH)_2@NF$ that the possible formation mechanism is as follows:



1



2



3

2.3 Characterization

In this study, all samples used for characterization are synthetic composite particles scraped from NF by stainless steel spoon. The crystallinity and phases of the materials were analyzed by X-ray diffraction (XRD) with Cu K α ($\lambda = 0.15418$ nm) radiation using D/max-2500 unit from Rigaku Co., Japan). Morphology and sizes of the materials were observed by the scanning electron microscope (SEM, JEOL, JSM-6360LA, Japan) and transmission electron microscope (TEM, FEI-G20). The Brunauer-Emmett-Teller (BET) surface area and pore size distribution of the catalyst was measured by using ASAP 2460 adsorption device from Micromeritics. To investigate the reactive species generated in the heterogeneous MnO₂/Ni(OH)₂@NF/PS system, ESR spectra were collected by ESR spectrometer (Bruker, EMX PLUS) to capture the different types of free radicals generated in the reaction system.

2.4 Catalytic degradation studies of Orange II

The prepared samples have been evaluated for degradation of orange II (OII) under different conditions using the following procedure. The degradation experiments were carried out in a 100 mL beaker containing 50 mL OII dye solution (30 mg/L) (Here, the sample dosage is a piece of MnO₂/Ni(OH)₂@NF material (Fig. 1 (c)), and the particles scraped off the surface are about 20 mg) while stirring with a magnetic stirrer at the rotating speed of 100 rpm, and the experimental temperature for dye degradation was 15 ± 2 °C. The initial solution pH was adjusted to the determined value by using NaOH (1 M) and HCl (3 M). Firstly, the prepared MnO₂/Ni(OH)₂@NF material was immersed in OII dye solution, and the degradation process was started by adding PS. After the reaction, about 1.5ml solution was extracted by syringe at regular time intervals, and then filtered by 0.22 μ m filter membrane. The filtered solution (1mL) was added into the colorimetric tube and diluted 10 times. The absorbance of OII dye at its maximum absorption wavelength of 484 nm was determined by UV-vis spectrophotometer. All the experiments were conducted in dark conditions and were repeated at least twice.

3 Results And Discussion

3.1 Characterization of material

The XRD patterns of prepared MnO₂/Ni(OH)₂@NF samples are presented in Fig. 2. The XRD pattern of the synthesized sample showed obvious characteristic diffraction peaks at about 44.3°, 51.8° and 76.3°, which can be indexed to the (111), (200) and (220) crystal planes of Ni, respectively. All the diffraction peaks of the sample are consistent with standard card (PDF#04-0850) for Ni. Besides, three characteristic diffraction peaks of Ni in the XRD pattern of the synthesized sample, there are also obvious characteristic diffraction peaks at 19.1°, 38.9° and 61.5°, which are indexed to (111), (222) and (511) crystal planes of MnO₂ (PDF#44-0992). In the XRD pattern of the synthesized sample, except for the characteristic diffraction peaks of Ni and MnO₂, there are also obvious diffraction peaks at 11.3°, 22.4°, 34.5°, 38.9° and 60.6°, which correspond to the (003), (006), (012), (015) and (113) crystal planes of Ni(OH)₂ (PDF#38-0715). No other characteristic peaks were found, confirming the above phases of the synthesized product.

The surface morphologies of $\text{MnO}_2/\text{Ni}(\text{OH})_2@\text{NF}$ were observed by SEM at different magnifications. As can be seen from Fig. 3, the overall framework of the material is in a network structure, petal-shaped particles are scattered on the surface of the flakes, and the pores between the flakes are large and evenly distributed. It can also be observed from Fig. 3b that flake nanosheets are very dense and evenly distributed. It shows that $\text{MnO}_2/\text{Ni}(\text{OH})_2$ composite material has been successfully deposited on the surface of NF. TEM images of $\text{MnO}_2/\text{Ni}(\text{OH})_2@\text{NF}$ sample are shown in Fig. 3(c,d). Its continuous lattice planes at different locations represent good crystallinity of different phases. The interplanar spacings are 0.779 nm, 0.464 nm, 0.203 nm, which correspond to (003), (111), (111) crystal plane of $\text{Ni}(\text{OH})_2$, MnO_2 , Ni, respectively. Figure 4 shows N_2 adsorption/desorption isotherm and pore size distribution of $\text{MnO}_2/\text{Ni}(\text{OH})_2$ scraped from NF surface. The BET surface area of $\text{MnO}_2/\text{Ni}(\text{OH})_2$ nanostructure is $5 \text{ m}^2/\text{g}$. According to IUPAC classification, the adsorption isotherm of the sample is type IV isotherm, and the adsorption H3 hysteresis loop appears in the middle section, and the pore size of the porous material is between 2–50 nm, which belongs to mesoporous material characteristics.

3.2 Preliminary study on degradation of OII

The degradation of OII in different systems is shown in Fig. 5. With only the NF (Fig. 1b) in the system, the degradation rate was 13.65%. It can be seen from Fig. 5 that the degradation rate is basically unchanged after 10 minutes, indicating that the adsorption-desorption equilibrium has been reached and the adsorption capacity of $\text{MnO}_2/\text{Ni}(\text{OH})_2@\text{NF}$ sample is obviously higher than that of NF. The degradation rate was 34.09% when only the oxidizing agent, PS was added into the above reaction system. When $\text{MnO}_2/\text{Ni}(\text{OH})_2@\text{NF}$ sample and PS were added to OII solution, we found that 98.68% of OII was degraded within 40 min.

3.3 Effect of PS dosage

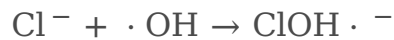
In the presence of $\text{MnO}_2/\text{Ni}(\text{OH})_2@\text{NF}$ catalyst, the degradation of OII under different PS dosages was investigated (Fig. 6). Without PS, because of the specific surface area of the catalyst, about 50% of OII was adsorbed on $\text{MnO}_2/\text{Ni}(\text{OH})_2@\text{NF}$ surface within 40 minutes. When $\text{MnO}_2/\text{Ni}(\text{OH})_2@\text{NF}$ and PS existed in the reaction system at the same time, it can be seen from Fig. 6 that with the increase of PS dosage from 1 g/L to 2 g/L, the degradation rate of OII was obviously improved, and this result is consistent with previous studies[18, 24, 25]. This may be due to PS accelerating activation for the generation of $\text{SO}_4^{\cdot-}$ -and $\cdot\text{OH}$ radicals. In addition, the electronic exchange Mn^{3+} , Mn^{4+} , Ni^{2+} , Ni^{3+} in MnO_2 and $\text{Ni}(\text{OH})_2$ may be another main reason for the catalytic reaction. However, the degradation of OII decreased with the further increase of PS dosage (3 g/L). This may be the scavenging effect of excessive PS quenching $\text{SO}_4^{\cdot-}$ (Eq. (8)) radicals^[26]. Therefore, 2 g/L appears to be the optimum dosage of PS for OII degradation.

3.4 Effect of initial solution pH

The effect of the initial solution pH from 3.0 to 11.0 on the OII degradation by $\text{MnO}_2/\text{Ni}(\text{OH})_2@\text{NF}/\text{PS}$ was investigated and the corresponding results are illustrated in Fig. 7. The initial pH of the solution plays an important role in the degradation of OII in heterogeneous catalysis. The results showed that with the increase of initial pH, the removal rate of OII decreased, which is consistent with the previously reported results[18, 25]. Obviously, acidic conditions are favorable for the formation of $\text{SO}_4^{\cdot-}/\cdot\text{OH}$ radicals as can be seen from Eq. (12) and the generated free radicals accelerate the degradation of OII. In addition, under acidic conditions, the redox potential of free radicals ($\text{SO}_4^{\cdot-}$ and $\cdot\text{OH}$) is relatively high, which also helps to promote the faster degradation of OII. With the initial pH increasing from 3.0 to 11.0, the removal rate of OII decreased from 98.96–74.22%.

3.5 Effect of inorganic anions

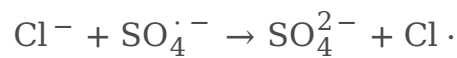
It is well known that inorganic anions in industrial wastewater, such as nitrate ion (NO_3^-) and chlorine ion (Cl^-), which can react with active free radicals at high reaction rates and hence this reaction with anions inhibits the degradation of pollutants. Therefore, the influences of inorganic anions such as NO_3^- and Cl^- on the catalytic degradation process of OII was evaluated and shown in Fig. 8. It can be seen from Fig. 8 that the existence of NO_3^- and Cl^- obviously reduced the degradation efficiency of OII, which is due to the fact that NO_3^- and Cl^- can react with free radicals to generate active substances with low activity, thus inhibiting the removal rate of OII (Eq. 4–9)[27].



4



5



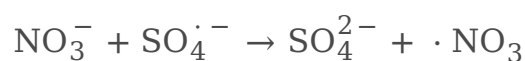
6



7



8



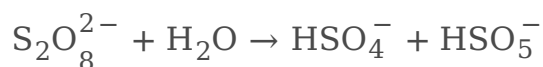
3.6 Material stability and recyclability

In order to evaluate the repeatability and stability of the catalyst, the whole $\text{MnO}_2/\text{Ni}(\text{OH})_2@\text{NF}$ catalyst material after degradation reaction was taken out of the solution. After rinsing with ultra-pure water, the used catalyst was cycled for the next reaction under the same reaction conditions. The cyclic degradation efficiency of OII solution by $\text{MnO}_2/\text{Ni}(\text{OH})_2@\text{NF}$ using the combination of $\text{MnO}_2/\text{Ni}(\text{OH})_2@\text{NF}$ and PS is depicted in Fig. 9. After three cycles, the degradation rate of OII could still reach 89.05%, which indicated that $\text{MnO}_2/\text{Ni}(\text{OH})_2@\text{NF}$ had good stability and high recoverability. It can be concluded that the high stability of $\text{MnO}_2/\text{Ni}(\text{OH})_2$ with three-dimensional hierarchical structure can effectively avoid the agglomeration phenomenon of nano-catalyst when it is used for many times.

3.7 Investigation of major free radicals

To study the free radicals produced in $\text{MnO}_2/\text{Ni}(\text{OH})_2@\text{NF}/\text{PS}$ system, scavenging experiments were carried out in the oxidation process (Fig. 10). As we all know, P-benzoquinone (BQ) was used as a unique quenchant for superoxide anion radical ($k = (0.9-1) \times 10^9 \text{ M}^{-1} \text{ s}^{-1}$). When excessive BQ content (2 mM) is added into the system, the inhibition can be neglected. This may be due to the extremely low yield of superoxide anion radicals ($\text{O}_2^{\cdot-}$) as well as their low reactivity to OII [28]. This indicates that $\text{O}_2^{\cdot-}$ radical could not be the main active species for OII degradation. Methanol (CH_3OH , MeOH) and tert-butyl alcohol (TBA) were used as the scavengers of the hydroxyl radicals ($\cdot\text{OH}$) and sulfate radicals ($\text{SO}_4^{\cdot-}$) and surface free radicals. However, the quenching effect of TBA on $\cdot\text{OH}$ is particularly good. It can be seen from Fig. 10 that compared with TBA, MeOH has a greater inhibitory effect on the degradation rate of OII. When TBA and MeOH were added into the system, the degradation rates of OII were 67.20% and 51.04%, respectively. Therefore, the main active species to degrade OII could be $\text{SO}_4^{\cdot-}$, and the conversion of $\text{SO}_4^{\cdot-}$ into $\cdot\text{OH}$ may lead to the outstanding contribution of $\cdot\text{OH}$ through (Eq. (13)).

Furthermore, ESR test with 5,5-dimethyl-1-pyrrolin-N-oxide (DMPO) as spin capture agent was also carried out. The catalyst powder scraped from NF was added into OII solution together with DMPO and PS. Within 5 minutes before the reaction, the characteristic peaks of $\cdot\text{OH}$ and $\text{SO}_4^{\cdot-}$ were DMPO- $\cdot\text{OH}$ and DMPO- $\text{SO}_4^{\cdot-}$ adducts (Fig. 11). Thus, it appears that $\cdot\text{OH}$ and $\text{SO}_4^{\cdot-}$ act together in this degradation reaction. Furthermore, it can be seen from Fig. 11 that the heights of the peaks are relatively high, indicating that the concentration of free radicals is also relatively high. It also verified the phenomenon of free radical scavenging experiments.





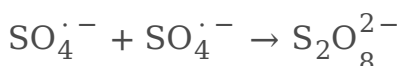
11



12



13



14



15

4 Conclusion

In this work, a rapid and mild green preparation technology was proposed for catalyst preparation. The results show that mesoporous materials are successfully formed in situ on the NF carrier at the reaction temperature of 90°C under hydrothermal condition and time of 3 hours. Through the free radical quenching experiments and ESR test, it was determined that the active species such as $\cdot\text{OH}$ and $\text{SO}_4^{\cdot-}$ were mainly produced during the activation of PS by $\text{MnO}_2/\text{Ni(OH)}_2@\text{NF}$ catalyst. The excellent degradation ability of the system may have potential application prospects in the catalytic oxidation of organic dyes or other organic pollutants.

Declarations

Declaration of Competing Interests

The authors declare that they have no known competing financial interests or personal relationships that could have appeared to influence the work reported in this paper.

Authors' contributions

Conceptualization, Data curation, Formal analysis, Funding acquisition, Investigation, Methodology, Project administration, Resources, Software, Supervision, Validation, Visualization, all by Prof. Jianfeng. Writing - original draft by Fang Zhu, Qixing Xiao and Yu Mei. Writing - review & editing by all authors, Fang Zhu, Qixing Xiao, Yu Mei, Zihao Hu, Jianfeng Ma and Sridhar Komarneni.

Acknowledgments

This work was supported by “Qing Lan Project” of Jiangsu Province, “333 Project” of Jiangsu Province, the Natural Science Foundation of Zhejiang Province (No. LGF20E020002) and innovation and entrepreneurship training program for college students in Jiangsu Province (No. 202110292062Y). The authors thank Shiyanjia lab (www.shiyanjia.com) for the support of ESR tests.

References

1. J. Qian, X. Gao, B. Pan, Nanoconfinement-mediated water treatment: from fundamental to application. *Environ. Sci. Technol.* **54**, 8509–8526 (2020). <https://doi.org/10.1021/acs.est.0c01065>
2. C. Song, Q. Zhan, F. Liu, C. Wang, H. Li, X. Wang, X. Guo, Y. Cheng, W. Sun, L. Wang, Overturned Loading of Inert CeO₂ to Active Co₃O₄ for Unusually Improved Catalytic Activity in Fenton-like Reactions, *Angewandte Chemie*. <https://doi.org/10.1002/ange.202200406>
3. B.C. Hodges, E.L. Cates, J.-H. Kim, Challenges and prospects of advanced oxidation water treatment processes using catalytic nanomaterials. *Nat. Nanotechnol.* **13**, 642–650 (2018)
4. B. Zhu, H. Cheng, Y. Qin, J. Ma, Y. Kong, S. Komarneni, Copper sulfide as an excellent co-catalyst with K₂S₂O₈ for dye decomposition in advanced oxidation process. *Sep. Purif. Technol.* **233**, 116057 (2020). <https://doi.org/10.1016/j.seppur.2019.116057>
5. F. Zhu, J. Ma, Q. Ji, H. Cheng, S. Komarneni, Visible-light-driven activation of sodium persulfate for accelerating orange II degradation using ZnMn₂O₄ photocatalyst. *Chemosphere* **278**, 130404 (2021). <https://doi.org/10.1016/j.chemosphere.2021.130404>
6. R. Dou, H. Cheng, J. Ma, Y. Qin, Y. Kong, S. Komarneni, Degradation of methylene blue by Co₃O₄ with activation of bisulfite. *Funct. Mater. Lett.* **13**, 2050016 (2020). <https://doi.org/10.1142/S1793604720500162>
7. B. Zhu, H. Cheng, J. Ma, Y. Kong, S. Komarneni, Efficient degradation of rhodamine B by magnetically separable ZnS–ZnFe₂O₄ composite with the synergistic effect from persulfate. *Chemosphere* **237**, 124547 (2019). <https://doi.org/10.1016/j.chemosphere.2019.124547>
8. Q. Zhao, Y. Zheng, C. Song, Q. Liu, N. Ji, D. Ma, X. Lu, Novel monolithic catalysts derived from in-situ decoration of Co₃O₄ and hierarchical Co₃O₄@ MnOx on Ni foam for VOC oxidation. *Appl. Catal. B* **265**, 118552 (2020). <https://doi.org/10.1016/j.apcatb.2019.118552>
9. A. Zhang, W. Zheng, Z. Yuan, J. Tian, L. Yue, R. Zheng, D. Wei, J. Liu, Hierarchical NiMn-layered double hydroxides@ CuO core-shell heterostructure in-situ generated on Cu (OH)₂ nanorod arrays for high performance supercapacitors. *Chem. Eng. J.* **380**, 122486 (2020). <https://doi.org/10.1016/j.cej.2019.122486>
10. X. Liu, Y. Liu, H. Qin, Z. Ye, X. Wei, W. Miao, D. Yang, S. Mao, *Selective Removal of Phenolic Compounds by Peroxydisulfate Activation: Inherent Role of Hydrophobicity and Interface ROS* (*Environmental Science & Technology*, 2022), <https://doi.org/10.1021/acs.est.1c07469>

11. W. Huang, M. Brigante, F. Wu, C. Mousty, K. Hanna, G. Mailhot, Assessment of the Fe(III)–EDDS Complex in Fenton-Like Processes: From the Radical Formation to the Degradation of Bisphenol A. *Environ. Sci. Technol.* **47**, 1952–1959 (2013). <https://doi.org/10.1021/es304502y>
12. F. Zhu, Q. Ji, Y. Lei, J. Ma, Q. Xiao, Y. Yang, S. Komarneni, Efficient degradation of orange II by core shell $\text{CoFe}_2\text{O}_4\text{-CeO}_2$ nanocomposite with the synergistic effect from sodium persulfate. *Chemosphere* **291**, 132765 (2022). <https://doi.org/10.1016/j.chemosphere.2021.132765>
13. R. Dou, H. Cheng, J. Ma, S. Komarneni, Manganese doped magnetic cobalt ferrite nanoparticles for dye degradation via a novel heterogeneous chemical catalysis. *Mater. Chem. Phys.* **240**, 122181 (2020). <https://doi.org/10.1016/j.matchemphys.2019.122181>
14. H. Liang, H. Sun, A. Patel, P. Shukla, Z. Zhu, S. Wang, Excellent performance of mesoporous $\text{Co}_3\text{O}_4/\text{MnO}_2$ nanoparticles in heterogeneous activation of peroxymonosulfate for phenol degradation in aqueous solutions. *Appl. Catal. B* **127**, 330–335 (2012). <https://doi.org/10.1016/j.apcatb.2012.09.001>
15. Y. Chen, K. Ma, J. Wang, Y. Gao, X. Zhu, W. Zhang, Catalytic activities of two different morphological nano- MnO_2 on the thermal decomposition of ammonium perchlorate. *Mater. Res. Bull.* **101**, 56–60 (2018). <https://doi.org/10.1016/j.materresbull.2018.01.013>
16. J. Deng, Y. Ge, C. Tan, H. Wang, Q. Li, S. Zhou, K. Zhang, Degradation of ciprofloxacin using $\alpha\text{-MnO}_2$ activated peroxymonosulfate process: Effect of water constituents, degradation intermediates and toxicity evaluation. *Chem. Eng. J.* **330**, 1390–1400 (2017). <https://doi.org/10.1016/j.cej.2017.07.137>
17. D. Yue, X. Qian, M. Ren, M. Fang, J. Jia, Y. Zhao, Secondary battery inspired α -nickel hydroxide as an efficient Ni-based heterogeneous catalyst for sulfate radical activation. *Sci. Bull.* **63**, 278–281 (2018). <https://doi.org/10.1016/j.scib.2018.02.002>
18. R. Yuan, Z. Jiang, Z. Wang, S. Gao, Z. Liu, M. Li, G. Boczkaj, Hierarchical MnO_2 nanoflowers blooming on 3D nickel foam: a novel micro-macro catalyst for peroxymonosulfate activation. *J. Colloid Interface Sci.* **571**, 142–154 (2020). <https://doi.org/10.1016/j.jcis.2020.03.041>
19. R. Yuan, L. Hu, P. Yu, H. Wang, Z. Wang, J. Fang, Nanostructured Co_3O_4 grown on nickel foam: An efficient and readily recyclable 3D catalyst for heterogeneous peroxymonosulfate activation. *Chemosphere* **198**, 204–215 (2018). <https://doi.org/10.1016/j.chemosphere.2018.01.135>
20. R. Yuan, M. Jiang, S. Gao, Z. Wang, H. Wang, G. Boczkaj, Z. Liu, J. Ma, Z. Li, 3D mesoporous $\alpha\text{-Co(OH)}_2$ nanosheets electrodeposited on nickel foam: A new generation of macroscopic cobalt-based hybrid for peroxymonosulfate activation. *Chem. Eng. J.* **380**, 122447 (2020). <https://doi.org/10.1016/j.cej.2019.122447>
21. F. Wang, Q. Zhou, G. Li, Q. Wang, Microwave preparation of 3D flower-like $\text{MnO}_2/\text{Ni(OH)}_2$ /nickel foam composite for high-performance supercapacitors. *J. Alloys Compd.* **700**, 185–190 (2017). <https://doi.org/10.1016/j.jallcom.2017.01.037>
22. Y. Khan, S. Hussain, F. Söderlind, P.-O. Käll, M.A. Abbasi, S.K. Durrani, Honeycomb $\beta\text{-Ni(OH)}_2$ films grown on 3D nickel foam substrates at low temperature. *Mater. Lett.* **69**, 37–40 (2012).

<https://doi.org/10.1016/j.matlet.2011.11.058>

23. X. Xiong, D. Ding, D. Chen, G. Waller, Y. Bu, Z. Wang, M. Liu, Three-dimensional ultrathin Ni(OH)₂ nanosheets grown on nickel foam for high-performance supercapacitors. *Nano Energy* **11**, 154–161 (2015). <https://doi.org/10.1016/j.nanoen.2014.10.029>
24. E. Saputra, S. Muhammad, H. Sun, H.-M. Ang, M.O. Tadé, S. Wang, Manganese oxides at different oxidation states for heterogeneous activation of peroxymonosulfate for phenol degradation in aqueous solutions. *Appl. Catal. B* **142**, 729–735 (2013). <https://doi.org/10.1016/j.apcatb.2013.06.004>
25. Y. Xiao, Y. Wang, Y. Xie, H. Ni, X. Li, Y. Zhang, T. Xie, *Shape-controllable synthesis of MnO₂ nanostructures from manganese-contained wastewater for phenol degradation by activating peroxymonosulphate: performance and mechanism* (*Environmental Technology*, 2018), <https://doi.org/10.1080/09593330.2018.1554708>
26. J. Chen, W.-D. Zhang, J.-S. Ye, Nonenzymatic electrochemical glucose sensor based on MnO₂/MWNTs nanocomposite. *Electrochem. Commun.* **10**, 1268–1271 (2008). <https://doi.org/10.1016/j.elecom.2008.06.022>
27. F. Zhu, S. Zhou, M. Sun, J. Ma, W. Zhang, K. Li, H. Cheng, S. Komarneni, Heterogeneous activation of persulfate by Mg doped Ni(OH)₂ for efficient degradation of phenol. *Chemosphere* **286**, 131647 (2022). <https://doi.org/10.1016/j.chemosphere.2021.131647>
28. R. Yuan, Z. Wang, Y. Hu, B. Wang, S. Gao, Probing the radical chemistry in UV/persulfate-based saline wastewater treatment: Kinetics modeling and byproducts identification. *Chemosphere* **109**, 106–112 (2014). <https://doi.org/10.1016/j.chemosphere.2014.03.007>

Figures

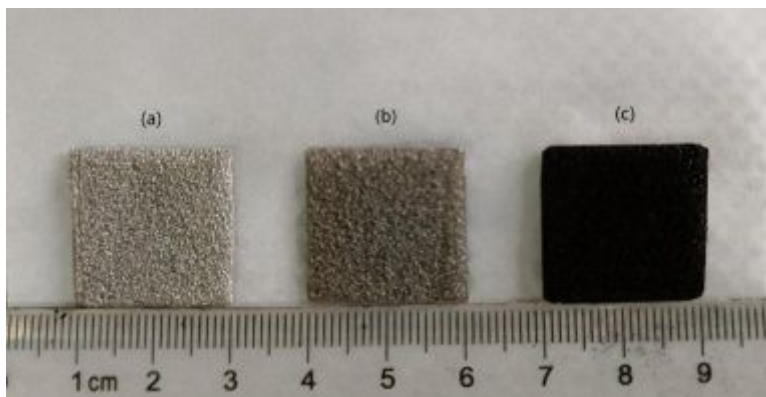


Figure 1

(a) 3D NF sheet, (b) 3D NF sheet after ultrasonic treatment, and (c) MnO₂/Ni(OH)₂@NF material at 90 °C.

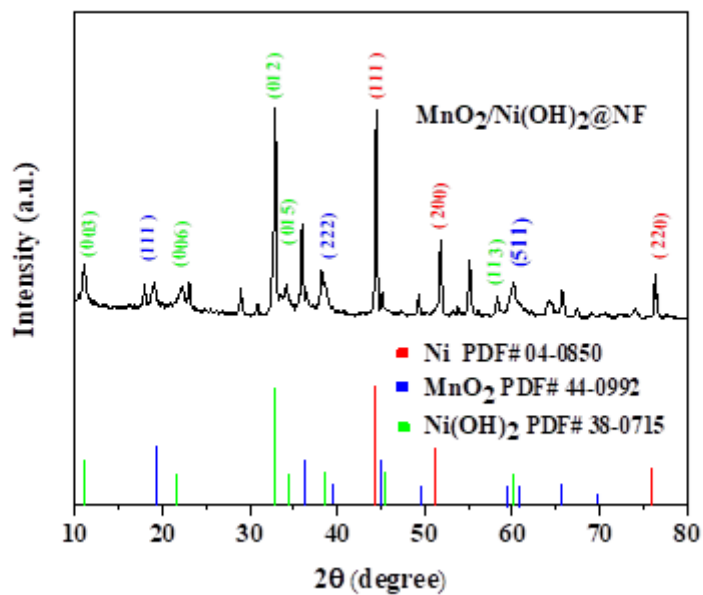


Figure 2

XRD pattern of $\text{MnO}_2/\text{Ni}(\text{OH})_2@\text{NF}$ sample.

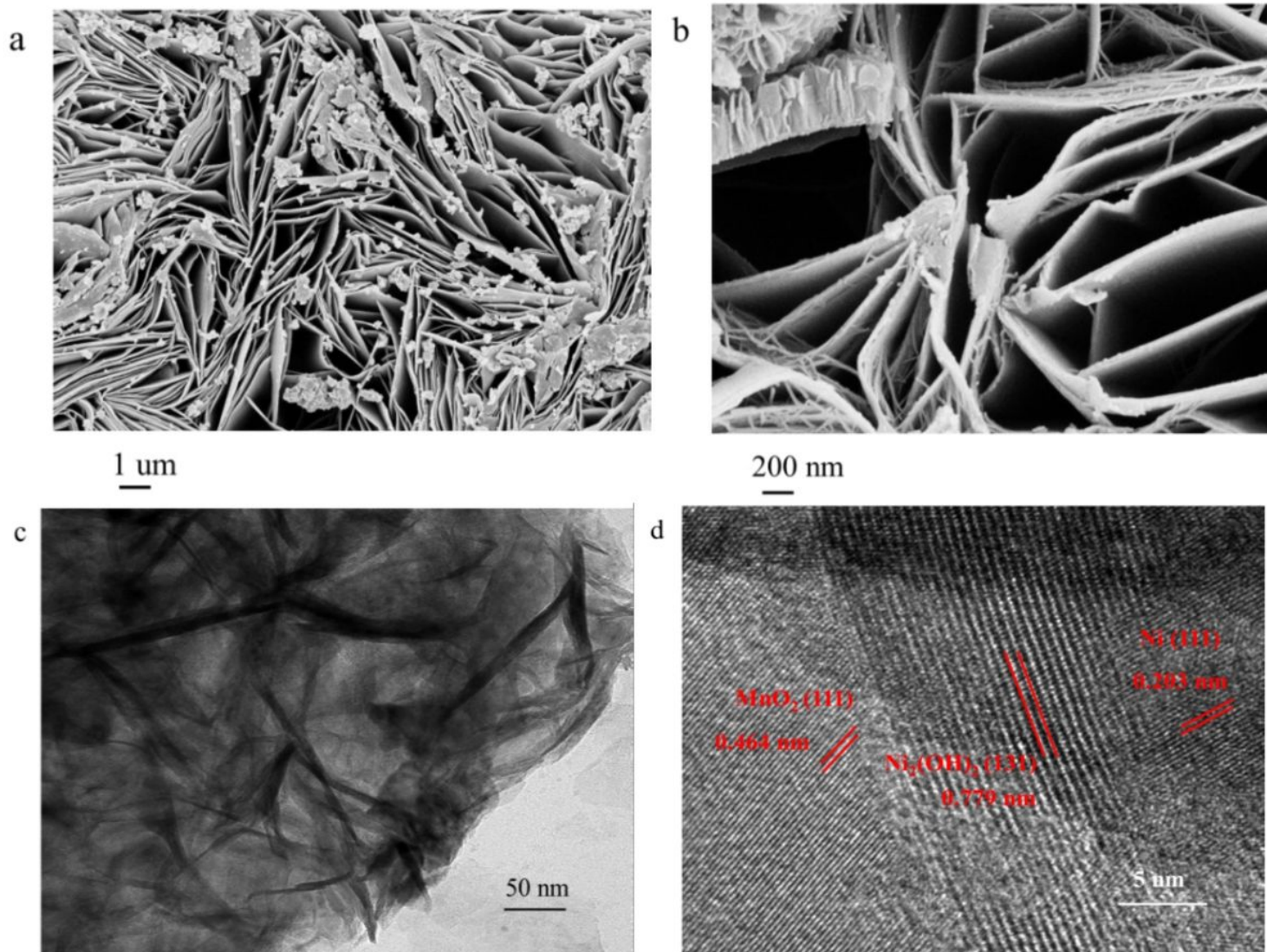


Figure 3

(a, b) SEM images of $\text{MnO}_2/\text{Ni}(\text{OH})_2@\text{NF}$ sample, (c, d) TEM images of $\text{MnO}_2/\text{Ni}(\text{OH})_2@\text{NF}$ sample.

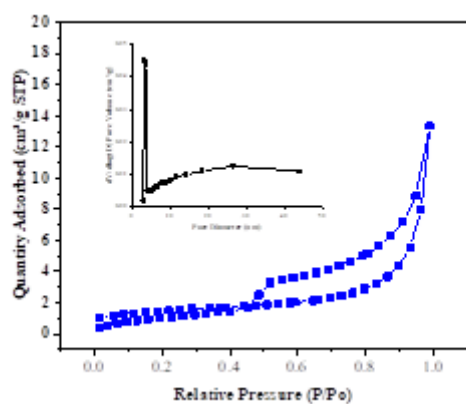


Figure 4

N_2 adsorption/desorption isotherms and pore size distribution (inset) of $MnO_2/Ni(OH)_2$ scraped from the surface of NF.

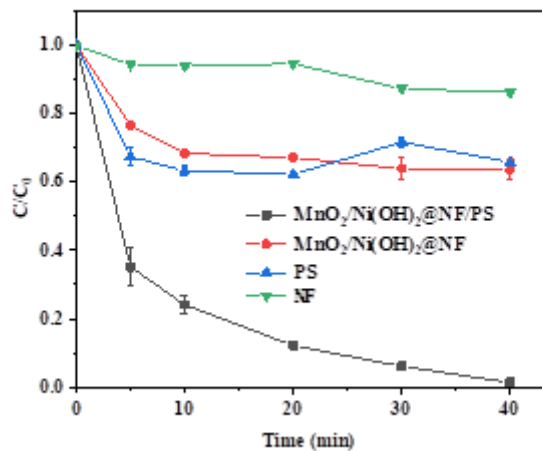


Figure 5

Oil degradation by $MnO_2/Ni(OH)_2@NF$ sample under different conditions. Experimental Conditions: orange II 30 mg/L, $K_2S_2O_8$ 2.0 g/L. Experimental conditions: [Oil] = 30 mg/L, [PS] = 2.0 g/L, [catalysts] = a piece of $MnO_2/Ni(OH)_2@NF$ material (Fig. 1 (c)).

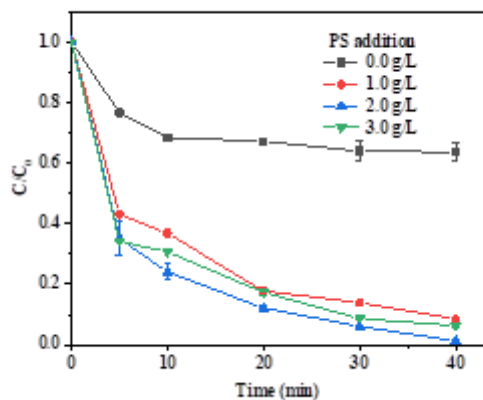


Figure 6

Effect of PS addition on the degradation of Oil in $MnO_2/Ni(OH)_2@NF/PS$ system. Experimental conditions: [Oil] = 30 mg/L, [PS] = 2.0 g/L, [catalysts] = a piece of $MnO_2/Ni(OH)_2@NF$ material (Fig. 1 (c)).

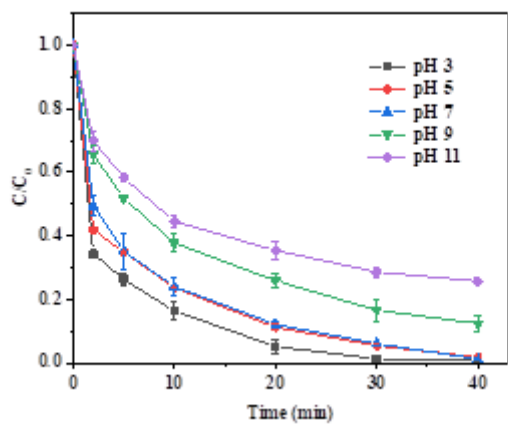


Figure 7

Effect of pH on the degradation of Oil in $\text{MnO}_2/\text{Ni}(\text{OH})_2@\text{NF}/\text{PS}$ system. Experimental conditions: $[\text{Oil}] = 30 \text{ mg/L}$, $[\text{PS}] = 2.0 \text{ g/L}$, $[\text{catalysts}] = \text{a piece of } \text{MnO}_2/\text{Ni}(\text{OH})_2@\text{NF} \text{ material (Fig. 1 (c))}$.

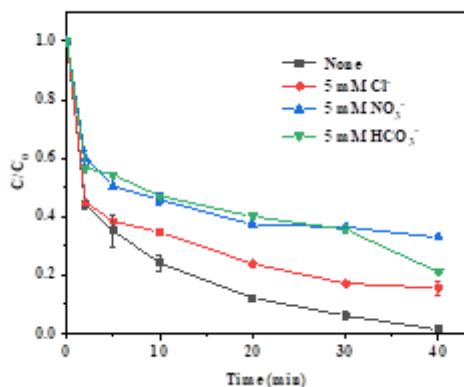


Figure 8

Effect of inorganic anions on the degradation of Oil in $\text{MnO}_2/\text{Ni}(\text{OH})_2@\text{NF}/\text{PS}$ system. Experimental conditions: $[\text{Oil}] = 30 \text{ mg/L}$, $[\text{PS}] = 2.0 \text{ g/L}$, $[\text{catalysts}] = \text{a piece of } \text{MnO}_2/\text{Ni}(\text{OH})_2@\text{NF} \text{ material (Fig. 1 (c))}$.

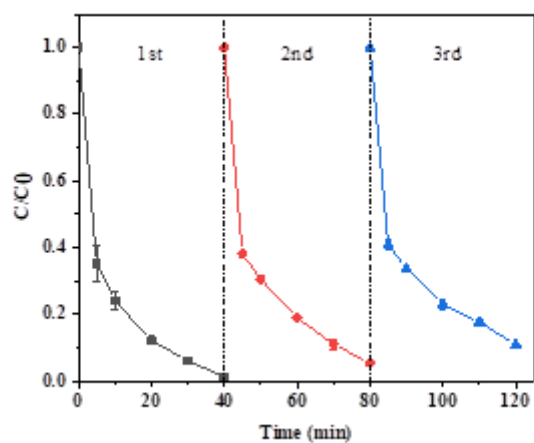


Figure 9

Degradation efficiencies of OII using the recycled material of MnO₂/Ni(OH)₂@NF. Experimental conditions: [OII] =30 mg/L, [PS] =2.0 g/L, [catalysts] = a piece of MnO₂/Ni(OH)₂@NF material (Fig. 1 (c)).

Figure 10

Effects of various scavengers on the degradation. Experimental conditions: [OII] =30 mg/L, [PS] =2.0 g/L, [catalysts] =20 mg of the particles scraped off the MnO₂/Ni(OH)₂@NF surface.

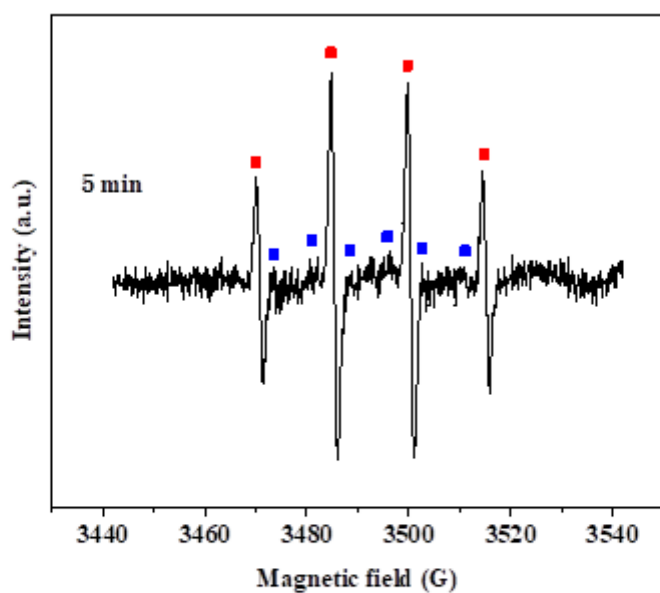


Fig. 11 ESR spectra of DMPO adducts (■:DMPO-•OH; ■: DMPO-SO₄^{•-}). Experimental conditions: [OII] =30 mg/L, [PS] =2.0 g/L, [catalysts] =20 mg of the particles scraped off the MnO₂/Ni(OH)₂@NF surface and [DMPO] = 50 mM.

Figure 11

See image above for figure legend.